Check for updates

From optical pumping to electrical pumping: the threshold overestimation in metal halide perovskites†

Jiajun Qin, [ID] [ab] Yang Tang,[a] Jia Zhang,[b] Tangyao Shen,[a] Max Karlsson,[b] Tiankai Zhang,[b] Weidong Cai,[b] Lei Shi,*[a] Wei-Xin Ni[b] and Feng Gao [ID] *[b]

The threshold carrier density, conventionally evaluated from optical pumping, is a key reference parameter towards electrically pumped lasers with the widely acknowledged assumption that optically excited charge carriers relax to the band edge through an ultrafast process. However, the characteristically slow carrier cooling in perovskites challenges this assumption. Here, we investigate the optical pumping of state-of-the-art bromide- and iodine-based perovskites. We find that the threshold decreases by one order of magnitude with decreasing excitation energy from 3.10 eV to 2.48 eV for methylammonium lead bromide perovskite (MAPbBr$_3$), indicating that the low-energy photon excitation facilitates faster cooling and hence enables efficient carrier accumulation for population inversion. Our results are then interpreted due to the coupling of phonon scattering in connection with the band structure of perovskites. This effect is further verified in the two-photon pumping process, where the carriers relax to the band edge with a smaller difference in phonon momentum that speeds up the carrier cooling process. Furthermore, by extrapolating the optical pumping threshold to the band edge excitation as an analog of the electrical carrier injection to the perovskite, we obtain a critical threshold carrier density of $\sim 1.9 \times 10^{17}$ cm^{-3}, which is one order of magnitude lower than that estimated from the conventional approach. Our work thus highlights the feasibility of metal halide perovskites for electrically pumped lasers.

New concepts

We challenge the conventional estimation of the threshold carrier density for stimulated emissions in perovskite materials using one single-wavelength photoexcitation, which we believe would lead to significant overestimation. This is because of the unique slow hot carrier cooling in metal halide perovskites—a process that is not reported in conventional semiconducting materials. By taking this largely ignored cooling process into consideration, the needed threshold carrier densities can be at a level of 10^{17} cm^{-3}, which is one order of magnitude lower than the previously reported estimate. Such a low threshold value makes perovskites comparable to the commercialized state-of-the-art inorganic semiconductor lasers, indicating a step further to develop electrically pumped lasers based on metal halide perovskites. Our research results unveil the following remarkable points. (1) The effect of hot carrier cooling on optically pumped amplified spontaneous emission (ASE) thresholds is observed as a universal phenomenon in both bromide- and iodine-based perovskite films. (2) The two-photon up-conversion ASE is also studied by introducing the excitation photon energies between $0.5E_g$ and $1.0E_g$. The cooling process becomes faster compared to one-photon excitation with the same energy.

1. Introduction

Metal halide perovskites have gained great attention because of their success in various optoelectronic applications, including solar cells,[1–3] photo detectors,[4,5] X-ray detectors,[6] optically pumped lasers[7,8] and light emitting diodes (LEDs).[9–11] With the recent demonstrations of continuous-wave optically pumped perovskite lasers at room temperature[12] and intense charge injection in perovskite LEDs,[13–15] there is a growing interest to develop solution-processed electrically pumped injection laser diodes—a topic that has challenged the field for over two decades—using perovskite semiconductors. For successful stimulated emission and eventual lasing, a low threshold carrier density for population inversion in the active medium is demanded and is a key parameter associated with many basic properties in the materials and device, such as carrier distributions near the band edges and absorption losses, *etc.*, but this has been less studied on the perovskites in detail in the literature.

The threshold carrier density of a material can be estimated from conventional optical pumping experiments.[16–19] However,

[a] State Key Laboratory of Surface Physics, Key Laboratory of Micro- and Nano-Photonic Structures (Ministry of Education) and Department of Physics, Fudan University, Shanghai 200433, China. E-mail: lshi@fudan.edu.cn

[b] Department of Physics, Chemistry, and Biology (IFM), Linköping University, Linköping SE-58183, Sweden. E-mail: feng.gao@liu.se

† Electronic supplementary information (ESI) available: Fig. S1–S8. See DOI: https://doi.org/10.1039/d2mh01382g

the estimates obtained by those measurements cannot be simply applied to metal halide perovskites. The slow cooling of hot carriers[20,21] excited to the high-energy bands delays the carrier accumulation for stimulated emission, consequently resulting in an over-estimated threshold carrier density.

Our work thus aims to find a rational way to estimate the required threshold carrier density that is useful for the design of electrically pumped perovskite laser diodes. We investigate the excitation photon energy dependence of amplified spontaneous emissions (ASE) in state-of-the-art bromide- and iodine-based perovskites. By reducing the excitation photon energy, we observe a large reduction of the threshold carrier density of ASEs and the pronounced bandgap renormalization (BGR) effect. We attribute our results to the carrier cooling process that is affected by the coupling of the phonon scattering, giving rise to changes in the time delay for the carrier to accumulate at the band edge. This mechanism is verified in the two-photon pumping process, where carrier cooling to the band edge is faster than one-photon excitation with the equivalent excitation energy due to the different momentum requirement in connection to the band structure. Based on the above results, we evaluate the threshold carrier density of metal halide perovskites to the band edge excitation, which is considered as a rational analog to direct carrier injection through the electrical pumping, by extrapolating the experimental data to the excitation energy close to the bandgap. The obtained estimate is one order of magnitude lower than the previously reported value.

2. Results and discussion

2.1 ASE threshold difference by different excitation photon energies

We observe that the ASE threshold is strongly dependent on the excitation photon energy on the state-of-the-art methylammonium lead bromide (MAPbBr$_3$) perovskite film, where two different excitation photon energies (3.10 eV (400 nm) and 2.48 eV (500 nm)) are firstly chosen for the fluence-dependent photoluminescence (PL) measurements. For the 3.10 eV excitation (Fig. 1a), at very low pump fluence (below 169.8 μJ/cm^2/pulse), a relatively broad spontaneous emission is observed with a peak at 2.29 eV (542 nm) and full width at half maximum (FWHM) of $\sim$95 meV ($\sim$20 nm). By increasing the pump fluence to over 215.0 μJ/cm^2/pulse, an additional sharp peak at around 2.27 eV (546 nm) arises with a spectral width of $\sim$25 meV and dominates at high pump fluence, which is a typical feature of ASE. The threshold value is determined to be 215.0 μJ/cm^2/pulse by combining the integrated PL intensities and FWHM results (Fig. 1b). For the 2.48 eV excitation (Fig. 1c), a similar PL evolution with increasing pump fluence is observed to that of the 3.10 eV excitation case. A significant difference is that the ASE threshold decreases to 19.8 μJ/cm^2/pulse (in Fig. 1d), which is one order of magnitude lower compared to the 3.10 eV excitation case. It indicates that decreasing the excitation energy can largely benefit the population inversion and the stimulated emission in metal halide perovskites.
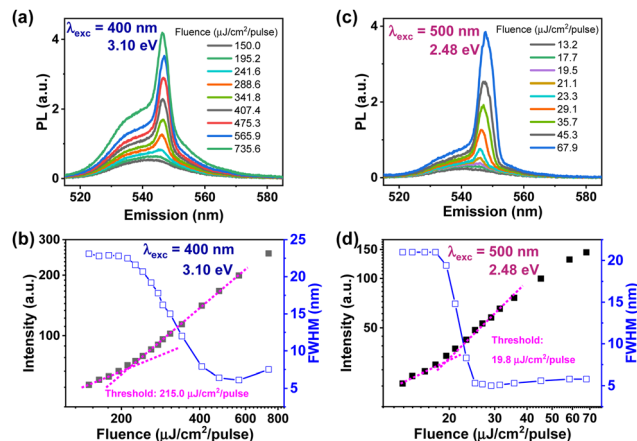

Fig. 1 Optically pumped ASE phenomenon in the MAPbBr$_3$ film under two different excitation photon energies. (a) Fluence–dependent PL spectra at the excitation photon energy of 3.10 eV (400 nm). (b) Integrated PL intensity and FWHM change with pump fluences at the excitation photon energy of 3.10 eV (400 nm). (c) Fluence-dependent PL spectra at the excitation wavelength of 2.48 eV (500 nm). (d) Integrated PL intensity and FWHM change with pump fluences at the excitation wavelength of 2.48 eV (500 nm).

Further studies on the excitation energy dependence of ASE threshold were carried out by systematically measuring the threshold values in a range of excitation photon energies between 3.10 eV (400 nm) and 2.48 eV (500 nm). The detailed fluence-dependent spectra for each excitation photon energy can be found in Fig. S1–S4 (ESI†), and there is also an overall summary in Fig. S5a (ESI†). For the excitation of 420 nm (2.95 eV), 440 nm (2.82 eV), 460 nm (2.70 eV), 480 nm (2.58 eV), the thresholds are 141.5, 90.5, 47.5, and 35.1 μJ/cm^2/pulse, respectively. We can calculate the threshold carrier densities for different excitation photon energies by considering the absorption coefficient (Fig. S5b, ESI†). As shown in Fig. 2a, the threshold carrier density decreases linearly with the excitation photon energy in a semi-logarithmic plot. For 3.10 eV excitation, the threshold carrier density is 1.0×10^{19} cm^{-3}, and for 2.70 eV is 1.4×10^{18} cm^{-3}. By further decreasing the excitation photon energy to 2.48 eV (an excitation wavelength seldomly used for bromide-based perovskites in the literature), the threshold carrier density can be further decreased to 5.1×10^{17} cm^{-3}. Following the trend and extending the excitation energy closer to the bandgap ($\sim$2.27 eV), which is the energy corresponding to the energy of injected electrons, the extrapolated threshold density is 1.9×10^{17} cm^{-3}. This value is nearly one order of magnitude lower than that previously reported from the optically pumped measurements.[22]

The observation of the excitation photon energy-dependent threshold carrier densities can be discussed by the schematic picture in Fig. 2b. The overall process involves three steps: (1) photon absorption (a very fast process in the order of femtoseconds), (2) hot carrier cooling/relaxation, and (3) carrier recombination. However, the cooling process is limited by coupling with multi-phonon emissions, and the scattering rate of phonons is approximately reciprocally proportional to the scalar
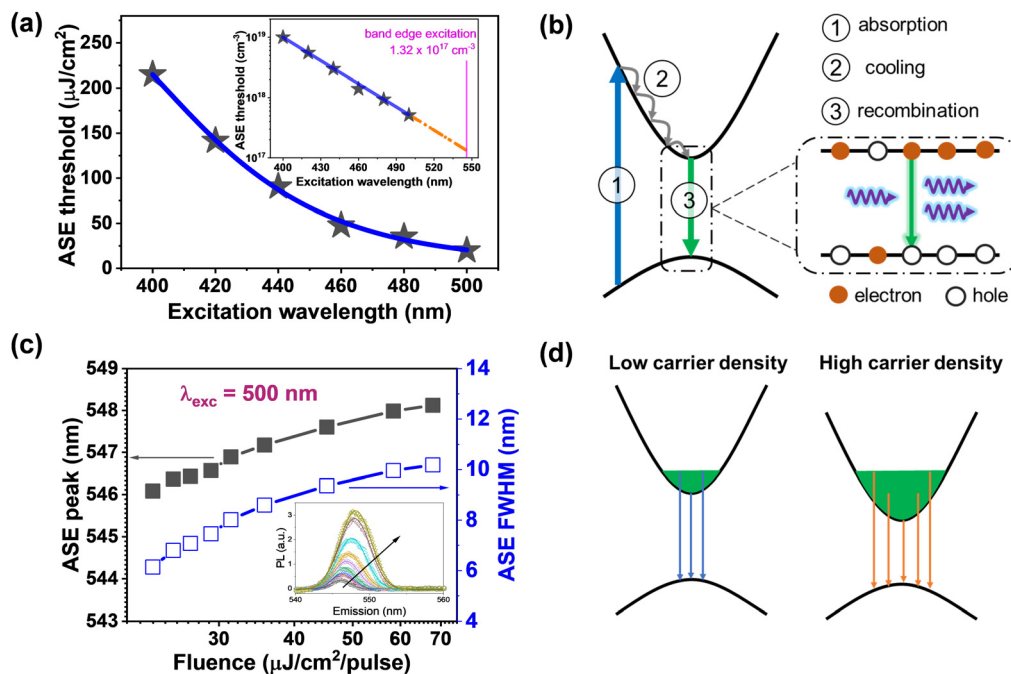
Fig. 2 Excitation photon energy-dependent optically pumped ASE phenomenon in the MAPbBr$_3$ film. (a) ASE threshold fluence and carrier density values at different excitation photon energies. The values are calculated with Fig. S5 (ESI†). (b) Schematic diagram to show the influence of the excitation photon energy on the ASE threshold. (c) The detailed information of the extracted ASE peaks (inset) at an excitation photon energy of 500 nm (2.48 eV). The black curve corresponds to the ASE peak position change, and the blue curve corresponds to the ASE FWHM change with pump fluence. (d) Schematic diagram of the BGR effect and filling caused by intense optical excitation. With increasing photoexcitation intensity, the BGR effect leads to a bandgap reduction, while the carrier filling at the band edge leads to a broadening of the emission peak.

value of the required momentum in each emission step.[23] A larger momentum difference results in a longer cooling time constant to reach the band edge, and thus a lower efficiency for carrier accumulation. Therefore, by decreasing the photoexcitation energy to make the initially excited states closer to the bottom of the band, i.e., the momentum difference becomes small, the cooling process will be largely facilitated. As a consequence, carriers can be more quickly accumulated and reach the population inversion with a lower threshold carrier density.

2.2 Evidence of carrier accumulation efficiency difference

The carrier accumulation due to quicker cooling is exemplified with the ASE spectral analysis excited at 2.48 eV (500 nm). For convenience, the broad spontaneous emission is subtracted, so that we can focus on the analysis of the ASE spectral evolution with pump fluence (Fig. 2c). Interestingly, when the pump fluence increases from 23.2 to 67.9 µJ/cm^2/pulse, the ASE peak position continuously redshifts from around 2.27 eV (546 nm) to 2.26 eV (548 nm). At the same time, the ASE FWHM also broadens from 25.5 meV to 42.0 meV. This combined phenomenon, i.e., ASE peak redshift and spectral width broadening, indicates the mechanism of BGR accompanied with band filling. A similar ASE spectral broadening and peak redshift phenomenon have also been observed in other perovskite systems, such as cesium lead bromide (CsPbBr$_3$) quantum dots[24] and nanocrystals.[25,26] As depicted in Fig. 2d, enhanced

Coulomb interaction at high carrier density (due to the reduction of average distance between the photogenerated charge carriers) will lead to a bandgap reduction owing to the BGR effect.[27,28] Therefore, the emission peak is expected to be redshifted. Again, owing to the high carrier density herein, the carriers will accumulate at the band edge as a result of band filling,[28] leading to a broadened emission spectrum. In this scenario, the bandgap reduction caused by the high carrier density, together with the band filling caused by carrier accumulation, leads to the ASE peak redshift and FWHM broadening simultaneously. In the case of the same bandgap reduction caused by the BGR effect, different cooling processes can result in differences in the carrier accumulation efficiency. Herein, a faster carrier cooling process to the band edge can lead to more efficient carrier accumulation, and hence a larger FWHM broadening.

Following this analysis, we can now compare the carrier accumulation efficiency at different excitation photon energies according to the relationship between the ASE peak and ASE FWHM in Fig. 3a. When the excitation photon energy decreases, the ASE FWHM increases for the same ASE peak, making the overall curve shifted towards the top-right (see excitation wavelength (energy) from 420 nm (2.95 eV) to 500 nm (2.48 eV)). This suggests that with a lower excitation photon energy, i.e., the excitation energy closer to the bandgap, the carrier accumulation is more efficient, which is consistent with the lower ASE threshold carrier density in Fig. 2a. It should
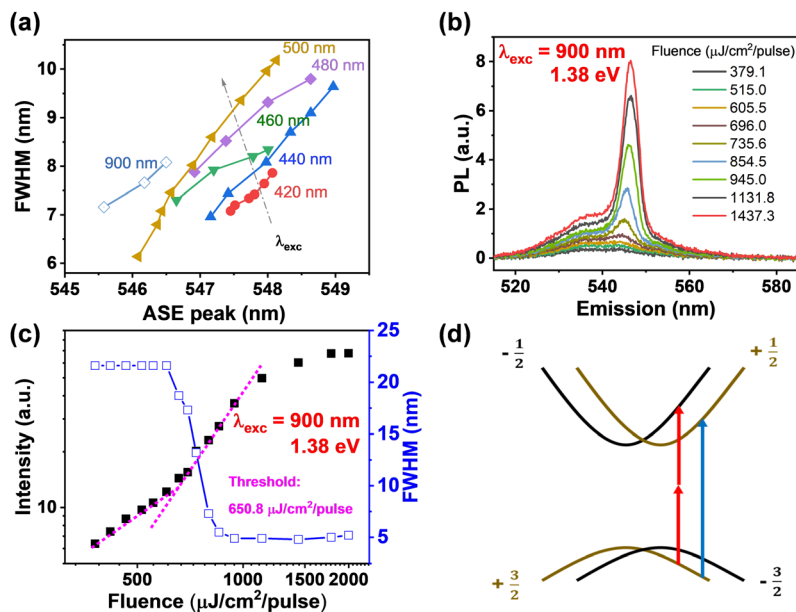
Fig. 3 Evidence of the fast carrier cooling process caused by low excitation photon energy. (a) Comparison of the ASE FWHM-ASE peak curves at different excitation photon energies (from 2.95 eV (420 nm) to 2.48 eV (500 nm) and even 1.38 eV (900 nm)). (b) Fluence-dependent PL spectra at an excitation wavelength of 900 nm. (c) Integrated PL intensity and FWHM change with pump fluences at an excitation wavelength of 900 nm. (d) Schematic diagram of the two-photon excitation process. Due to the selection rule, the two-photon absorption excites to a higher energy band beyond the one-photon transition, and is then followed by an intraband transition, which bypasses the carrier cooling process before recombination.

be noted that by simply tracking the FWHM *versus* peak plot, our ASE spectral analysis presents a convenient method to evaluate the carrier accumulation/carrier cooling efficiency.

2.3 Efficient carrier accumulation for two-photon upconversion ASE

We can further explore the carrier accumulation in the two-photon upconversion case, where the excitation photon energy is tuned to be 1.38 eV (900 nm) (smaller than $1.0E_g$, but larger than $0.5E_g$ of the perovskites). Owing to the relatively small cross section for the two-photon absorption process compared to the one-photon absorption process, the 1.38 eV excitation case shows a relatively large ASE threshold pump fluence value of 650.8 μJ/cm^2/pulse (Fig. 3b and c). Surprisingly, the FWHM-ASE peak curve of the 1.38 eV case (Fig. 3a) shifts even further towards the top-left than the 2.48 eV excitation case. This indicates that carrier accumulation is much more efficient than any of the one-photon excitation cases that we measured (3.1 eV to 2.48 eV), indicating that the carrier cooling through the two-photon process is much faster. For further confirmation, an excitation photon energy of 1.55 eV (refer to 800 nm) is also applied, and the ASE spectra are plotted in Fig. S6a (ESI†). The comparison of the FWHM-ASE peak relation was also plotted in Fig. S6b (ESI†). The similar top-right location of 1.55 eV case to that of 1.38 eV case in the figure indicates the universality that the two-photon up conversion process leads to a much faster carrier accumulation rate than any of the characterized one-photon excitation cases.

The fast-cooling process with the two-photon excitation is associated with the special band structure in metal halide perovskites, as depicted in Fig. 3d. Due to spin–orbit interaction

and lack of inversion-symmetry of the crystal potential, Rashba band splitting has been observed in perovskites.[29] Although the crystal bulk of our MAPbBr$_3$ perovskite is a centrosymmetrical structure,[30] symmetry breaking can still occur for the Rashba splitting effect in the polycrystalline thin film based on the following considerations: (1) symmetry breaking forms at the perovskite interface due to the asymmetric perovskite/ambient layout, as evidenced by many different experimental characterizations based on the MAPbBr$_3$ single crystal, *e.g.*, angle-resolved photoemission (ARPES) results[31] and circular photo-galvanic effect together with spatially resolved photoinduced inverse spin Hall effect measurements;[32] (2) the PbBr$_6$ octahedral thermal polar distortions at elevated temperatures can lead to a dynamical Rashba splitting effect;[33] (3) the strain inside the perovskite thin film can cause PbBr$_6$ octahedral distortion, increasing the possibility of the Rashba splitting effect.[34] Such unique band structure enables the two-photon absorption process that excites the electrons into a high energy band with opposite spins following the selection rule $\Delta J = \pm 2$, while the one-photon absorption only occurs between two bands with the same spin ($\Delta J = \pm 1$). As the momentum difference for cooling is smaller, the relaxation of the carriers excited *via* two-photon absorption to the bottom of the band is much faster compared to one-photon absorption with the same energy. This scenario is thus consistent with our experimental results shown in Fig. 3a.

2.4 Dynamics of carrier cooling and accumulation processes

The above discussions regarding the cooling process and carrier accumulation efficiency are based on the quasi-steady-state ASE analysis, including the threshold, peak and FWHM.

We then examine the effect of carrier cooling on the ASE threshold by studying the carrier dynamics of these processes *via* transient absorption (TA) measurements. As shown in Fig. 4a and b, when the excitation photon energy is 3.10 eV with the pump fluence of 565.9 μJ/cm^2/pulse (above the ASE threshold), the initial (delay time of 1 ps) photobleaching signal is mainly located at ∼2.48 eV. This high-energy photobleaching signal is strong evidence of the existence of hot carriers. The photobleaching peak gradually redshifts with the delay time, indicating a relatively slow cooling process. By contrast, in the 2.58 eV excitation case, the initial photobleaching peak is located at ∼2.38 eV, indicating that the carriers are much less hot than those generated by 3.10 eV excitation. The high-energy photobleaching signals decrease quickly within only several picoseconds (Fig. 4c), revealing a much faster cooling process. These observations match well with our above experimental results of low threshold carrier density and efficient carrier accumulation for low-energy photon excitation.

When the photoexcitation energy is 1.55 eV (800 nm) (Fig. 4e), *i.e.*, a two-photon process, the TA results are quite different from the corresponding one-photon excitation (400 nm) in Fig. 4a–d. There appears a significant photo-induced absorption signal without obvious photobleaching at a delay time of 0.8 ps. It indicates that the two-photon absorption process generates carriers somewhere beyond the conventional one-photon transition bands initially, which is consistent with the transition diagram in Fig. 3d. With increasing delay

time, a photobleaching signal with the peak at ∼2.36 eV starts to rise and reaches the maximum at 1.4 ps, suggesting that the timescale of carrier accumulation under two-photon excitation is very fast. Benefiting from the fast carrier accumulation, the carrier density at the band edge can increase instantly to exceed the threshold of population inversion. Thus, stimulated emission occurs, consistent with the fast-photobleaching signal decay of close to or less than 1 ps.

It should be noted that in the other bromide-based dense perovskite film system, a lower ASE threshold fluence for 1.55 eV (800 nm) excitation than that for 3.1 eV (400 nm) excitation[35] is reported. Moreover, in our previous perovskite system with monodispersed micrometer-sized large grains, only a two-photon up conversion (800 nm) excitation ASE is observed,[36] while for the one-photon (400 nm) excitation case, no ASE was observed in the same perovskite system.[37] Here, we reveal that the fast carrier cooling by the two-photon absorption process is responsible for the rather low required ASE threshold carrier density, which is highly promising for developing the two-photon absorption lasers based on metal halide perovskites.

2.5 Extension to iodine-based perovskite system

In order to verify the universality of our discovery that decreasing the excitation photon energy can lead to reduced threshold carrier densities in metal halide perovskites, we also measured the excitation photon energy-dependent PL of the state-of-the-
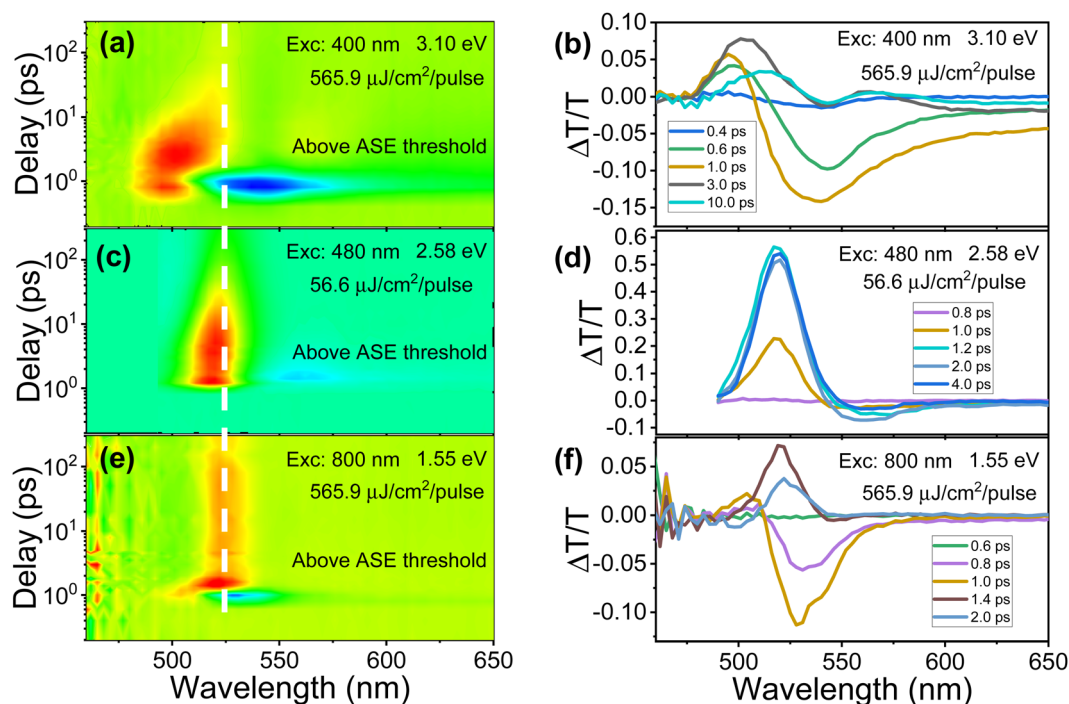

Fig. 4 TA results of the MAPbBr$_3$ film at different excitation photon energies. (a) Time evolution of the TA spectra at 3.10 eV (400 nm) excitation with the fluence of 565.9 μJ/cm^2/pulse, and (b) TA spectra at selected time delays: 0.4 ps, 0.6 ps, 1.0 ps, 3.0 ps and 10.0 ps. (c) Time evolution of TA spectra at 2.58 eV (480 nm) excitation with the fluence of 56.6 μJ/cm^2/pulse, and (d) TA spectra at selected time delays: 0.8 ps, 1.0 ps, 1.2 ps, 2.0 ps and 4.0 ps. (e) Time evolution of the TA spectra at 1.55 eV (800 nm) excitation with the fluence of 565.9 μJ/cm^{-2}/pulse, and (f) TA spectra at selected time delays: 0.6 ps, 0.8 ps, 1.0 ps, 1.4 ps and 2.0 ps.

art formamidinium lead iodide (FAPbI$_3$) film, which is widely used for both solar cells and LEDs. Consistent with the MAPbBr$_3$ films, a similar ASE threshold trend is observed by varying the excitation photon energies. As shown in Fig. S7 (ESI†), when the excitation photon energy is above 2.48 eV (500 nm), no ASE is observed up to a high pump fluence of 616.8 μJ/cm^2/pulse, suggesting a very high threshold. The ASE starts to appear when the excitation photon energy is changed to 2.25 eV (550 nm) with the threshold value of 100.7 μJ/cm^2/pulse. Upon further reduction of the excitation photon energy to 2.07 eV (600 nm) and 1.91 eV (650 nm), the threshold is reduced to 62.8 and 43.6 μJ/cm^2/pulse, respectively. By taking the absorption into consideration (Fig. S8a, ESI†), the threshold carrier densities at different excitation photon energies are calculated in Fig. S8b (ESI†). The extrapolation to the close-to-band-edge-excitation energy (1.51 eV (820 nm)) indicates that the theoretical threshold carrier density for population inversion by electrical injection in the FAPbI$_3$ film is 1.5×10^{17} cm^{-3}, a value similar to that for the MAPbBr$_3$ film.

3. Conclusions

In summary, we explore the effects of the excitation photon energy on the optically pumped ASE process in both one-photon and two-photon excitations. Our results confirm that a reduced ASE threshold can be achieved by using photoexcitation with the energy close to the bandgap energy. This is because of the fast carrier cooling that leads to an effective carrier accumulation for population inversion. The extrapolated threshold values for the resonance excitation, which corresponds to the eventual threshold carrier densities required for the electrical injection laser diodes, are one order of magnitude lower than the previous estimate based on optically pumped ASE experiments with only one specific excitation energy (wavelength) in both MAPbBr$_3$ and FAPbI$_3$ films. Our work thus infers a large potential and feasibility for the realization of electrically pumped metal halide perovskite lasers. Furthermore, the two-photon up-conversion photoexcitation is found to be energetically favorable for the faster cooling process required for carrier accumulation, as evidenced by both spectral analysis and TA results, which also opens up a great possibility for manufacturing the up-conversion lasers based on metal halide perovskite materials with a large application interest.

4. Experimental

4.1   Materials

Dimethyl sulfoxide (DMSO), dimethylformamide (DMF), lead acetate trihydrate (PbAc$_2$·3H$_2$O), lead bromide (PbBr$_2$), lead iodide (PbI$_2$), chlorobenzene (CB), *tert*-butanol (*t*-BuOH) and ethanol were purchased from Sigma–Aldrich. Formamidinium iodide (FAI), *n*-octylammonium iodide (OAI) and methylammonium bromide (MABr) were purchased from Greatcell Solar Materials. Tin oxide (SnO$_2$) nanoparticle water solution was

from Alfa Aesar. Poly(3,4-ethylenedioxythiophene):poly(styrene-sulfonate) (PEDOT:PSS, AI 4083) was from Heraeus. Methylammonium chloride (MACl) was from Xi'an Polymer Light Technology. All materials above were used without further purification.

4.2   Films fabrication

Substrate preparation: all films were spin-coated onto indium tin oxide (ITO) glass substrates. The substrates were cleaned by ultrasonication with detergent (1 time), deionized water (2 times) and ethanol (1 time). The time for each ultrasonication is at least 15 min. To prepare MAPbBr$_3$ films, an additional transport layer PEDOT:PSS was spin-coated first for better wettability of the perovskite precursor solutions. The PEDOT:PSS was spin-coated onto UV-ozone treated ITO substrate (for 15 min) with the spin speed of 4000 rpm for 40 s, followed by annealing at 150 °C for 20 min in air. To prepare FAPbI$_3$ films, the SnO$_2$ layer was coated prior to perovskite coating. The SnO$_2$ nanoparticle water solution was diluted with deionized water with a volume ratio of 1 : 6 (solution to water) and spin-coated at 4000 rpm for 40 s, followed by annealing at 150 °C for 30 min in air. After these steps, the pre-prepared substrates were transferred into the nitrogen glovebox.

MAPbBr$_3$ film preparation: first, three solutions were prepared individually: solution A with 0.3552 g PbAc$_2$·3H$_2$O and 0.4704 g MABr in 1 mL DMF; solution B with 0.5620 g PbBr$_2$ and 0.1796 g MABr in 1 mL DMF; solution C with 0.5620 g PbBr$_2$ and 0.1796 g MABr in 1 mL DMSO. Second, these three solutions were mixed with a volume ratio of 1 : 3.6 : 0.4 ($A:B:C$) to prepare the desired perovskite films. Third, 50 μL of the mixed solution was dropped onto PEDOT:PSS layers for subsequent spin-coating at the rate of 3000 rpm, followed by annealing at 60 °C for 30 min. The film samples were encapsulated with a glass by UV glue.

FAPbI$_3$ film preparation: the perovskite solution was prepared by mixing 1.81 M PbI$_2$, 1.65 M FAI, 0.58 M MACl in DMF and DMSO mixed solvent with the volume ratio of 8 : 1 mixed solution. After 50 μL of the solution was dropped onto SnO$_2$, spin-coating started at 5000 rpm for 30 s (2000 rpm ramping), and the surface was finished with 100 μL of CB as the anti-solvent onto the film at the same spin speed for ≤10 s. After spin-coating, the perovskite film was then annealed at 150 °C for 15 min in ambient air. Finally, 5 mg mL^{-1} OAI solution in *t*-BuOH was spin-coated onto the perovskite surface at 4000 rpm, and annealed at 100 °C for 3 min for surface passivation.

4.3   Film characterization

4.3.1   Femtosecond laser generation. A continuous-wave green laser (peaked at 532 nm) is initiated by Verdi V-10 (Coherent) as a source. The green laser is transformed into an ultrashort pulsed laser (wavelength of 800 nm, fluence of ~2 W, repetition frequency of 76 MHz) by Mira model 900 (Coherent). Then, the laser is amplified by Legend Elite (Coherent), converting into vertically polarized 800 nm pulsed laser with an output fluence of ~5 W and repetition frequency of 1 kHz. After passing through an optical parametric amplifier (OPA, from OPerA-Solo (Coherent)), a femtosecond laser with

desirable wavelength ranging from 285 nm to $\sim$2824.7 nm can be obtained.

4.3.2 ASE characterizations. The femtosecond laser light passes through one Glan Taylor Polarizer and one vertically polarized linear polarizer. By changing the polarization direction of the Glan Taylor polarizer, the final output power of the laser light can be altered. The power is monitored by a power meter (model: S120VC from Thorlabs). A focal lens is placed in between the linear polarizer and the perovskite sample to ensure a fixed beam size of 150 μm in diameter for excitation. The light is excited from the top surface of the film. The photoluminescence is collected from the other side of the sample by a spectroscopy (Horiba iHR320).

4.3.3 TA measurement. Laser light from Legend Elite is divided by a beam splitter. One part is reflected into the OperA Solo to generate light with different wavelengths of pumping, and another part is directed on the Ti:sapphire crystal to generate a broadband white light pulse as a probe light.

4.3.4 Other measurements. The absorption spectra were measured by a PerkinElmer Lambda 20 UV/VIS Spectrophotometer with an integrating sphere. The results were collected by transmission mode, where the samples were placed in front of the integrating sphere.

4.4 Carrier density calculation

The carrier density n is calculated based on the following equation:

$$n = (1 - R)(1 - e^{-\alpha d})\frac{\alpha \cdot I_{ps}}{\frac{hc}{\lambda}} \tag{1}$$

where I_{ps} is the pump fluence of one single pulse duration (in unit of μJ cm^{-2}), R is the reflection, α is the absorption coefficient, λ is the excitation wavelength, h is Planck's constant, and c is the speed of light. Here, I_{ps} is calculated by considering the area of the laser spot, the average power and the repetition rate. α is obtained by considering the absorption results and the film thickness.

Author contributions

Jiajun Qin conceived the idea and designed the experiments. Jiajun Qin and Jia Zhang synthesized the MAPbBr$_3$ perovskite films, and Tiankai Zhang synthesized the FAPbI$_3$ perovskite films. Yang Tang and Tangyao Shen carried out the PL and TA characterizations under the supervision of Lei Shi, and Jiajun Qin performed the data analysis. Jiajun Qin and Wei-Xin Ni perform the theoretical analysis. Jia Zhang, Max Karlsson and Weidong Cai contributed to the discussion. Jiajun Qin wrote the paper. Wei-Xin Ni and Feng Gao provided revisions. Feng Gao supervised the work. Jiajun Qin and Yang Tang contributed equally to this work. All authors contributed to this work, commented on the paper, and agreed to the contents of the paper and supplementary materials.

Conflicts of interest

There are no conflicts to declare.

Acknowledgements

References

1 R. Azmi, E. Ugur, A. Seitkhan, F. Aljamaan, A. S. Subbiah, J. Liu, G. T. Harrison, M. I. Nugraha, M. K. Eswaran, M. Babics, Y. Chen, F. Xu, T. G. Allen, A. Rehman, C. Wang, T. D. Anthopoulos, U. Schwingenschlögl, M. De Bastiani, E. Aydin and S. De Wolf, *Science*, 2022, **5784**, 1–9.

2 J. Jeong, M. Kim, J. Seo, H. Lu, P. Ahlawat, A. Mishra, Y. Yang, M. A. Hope, F. T. Eickemeyer, M. Kim, Y. J. Yoon, I. W. Choi, B. P. Darwich, S. J. Choi, Y. Jo, J. H. Lee, B. Walker, S. M. Zakeeruddin, L. Emsley, U. Rothlisberger, A. Hagfeldt, D. S. Kim, M. Grätzel and J. Y. Kim, *Nature*, 2021, **592**, 381–385.

3 J. J. Yoo, G. Seo, M. R. Chua, T. G. Park, Y. Lu, F. Rotermund, Y. K. Kim, C. S. Moon, N. J. Jeon, J. P. Correa-Baena, V. Bulović, S. S. Shin, M. G. Bawendi and J. Seo, *Nature*, 2021, **590**, 587–593.

4 X. Hu, X. Zhang, L. Liang, J. Bao, S. Li, W. Yang and Y. Xie, *Adv. Funct. Mater.*, 2014, **24**, 7373–7380.

5 L. Dou, Y. M. Yang, J. You, Z. Hong, W. H. Chang, G. Li and Y. Yang, *Nat. Commun.*, 2014, **5**, 5404.

6 Y. C. Kim, K. H. Kim, D. Y. Son, D. N. Jeong, J. Y. Seo, Y. S. Choi, I. T. Han, S. Y. Lee and N. G. Park, *Nature*, 2017, **550**, 87–91.

7 Q. Zhang, Q. Shang, R. Su, T. T. H. Do and Q. Xiong, *Nano Lett.*, 2021, **21**, 1903–1914.

8 K. Roh, L. Zhao and B. P. Rand, *ACS Photonics*, 2021, **8**, 2548–2554.

9 K. Lin, J. Xing, L. N. Quan, F. P. G. de Arquer, X. Gong, J. Lu, L. Xie, W. Zhao, D. Zhang, C. Yan, W. Li, X. Liu, Y. Lu, J. Kirman, E. H. Sargent, Q. Xiong and Z. Wei, *Nature*, 2018, **562**, 245–248.

10 Y. Cao, N. Wang, H. Tian, J. Guo, Y. Wei, H. Chen, Y. Miao, W. Zou, K. Pan, Y. He, H. Cao, Y. Ke, M. Xu, Y. Wang, M. Yang, K. Du, Z. Fu, D. Kong, D. Dai, Y. Jin, G. Li, H. Li, Q. Peng, J. Wang and W. Huang, *Nature*, 2018, **562**, 249–253.

11 W. Xu, Q. Hu, S. Bai, C. Bao, Y. Miao, Z. Yuan, T. Borzda, A. J. Barker, E. Tyukalova, Z. Hu, M. Kawecki, H. Wang, Z. Yan, X. Liu, X. Shi, K. Uvdal, M. Fahlman, W. Zhang, M. Duchamp, J. M. Liu, A. Petrozza, J. Wang, L. M. Liu, W. Huang and F. Gao, *Nat. Photonics*, 2019, **13**, 418–424.

12 C. Qin, A. S. D. Sandanayaka, C. Zhao, T. Matsushima, D. Zhang, T. Fujihara and C. Adachi, *Nature*, 2020, **585**, 53–57.

13 H. Kim, L. Zhao, J. S. Price, A. J. Grede, K. Roh, A. N. Brigeman, M. Lopez, B. P. Rand and N. C. Giebink, *Nat. Commun.*, 2018, **9**, 4893.

14 L. Zhao, K. Roh, S. Kacmoli, K. Al Kurdi, X. Liu, S. Barlow, S. R. Marder, C. Gmachl and B. P. Rand, *Adv. Mater.*, 2021, **33**, 2104867.

15 C. Zou, Y. Liu, D. S. Ginger and L. Y. Lin, *ACS Nano*, 2020, **14**, 6076–6086.

16 D. Saxena, S. Mokkapati, P. Parkinson, N. Jiang, Q. Gao, H. H. Tan and C. Jagadish, *Nat. Photonics*, 2013, **7**, 963–968.

17 S. Bao, D. Kim, C. Onwukaeme, S. Gupta, K. Saraswat, K. H. Lee, Y. Kim, D. Min, Y. Jung, H. Qiu, H. Wang, E. A. Fitzgerald, C. S. Tan and D. Nam, *Nat. Commun.*, 2017, **8**, 1845–1851.

18 R. Kirste, Q. Guo, J. H. Dycus, A. Franke, S. Mita, B. Sarkar, P. Reddy, J. M. LeBeau, R. Collazo and Z. Sitar, *Appl. Phys. Express*, 2018, **11**, 082101.

19 N. C. Giebink and S. R. Forrest, *Phys. Rev. B: Condens. Matter Mater. Phys.*, 2009, **79**, 1–4.

20 J. Fu, Q. Xu, G. Han, B. Wu, C. H. A. Huan, M. L. Leek and T. C. Sum, *Nat. Commun.*, 2017, **8**, 1300.

21 Y. Yang, D. P. Ostrowski, R. M. France, K. Zhu, J. Van De Lagemaat, J. M. Luther and M. C. Beard, *Nat. Photonics*, 2016, **10**, 53–59.

22 J. Qin, X. K. Liu, C. Yin and F. Gao, *Trends Chem.*, 2021, **3**, 34–46.

23 K. W. Böer, *Survey of semiconductor physics*, New York, 2nd edn, 2002.

24 D. Yan, T. Shi, Z. Zang, T. Zhou, Z. Liu, Z. Zhang, J. Du, Y. Leng and X. Tang, *Small*, 2019, **15**, 1–11.

25 C. Cho, A. Palatnik, M. Sudzius, R. Grodofzig, F. Nehm and K. Leo, *ACS Appl. Mater. Interfaces*, 2020, **12**, 35242–35249.

26 J. Navarro-Arenas, I. Suárez, V. S. Chirvony, A. F. Gualdrón-Reyes, I. Mora-Seró and J. Martínez-Pastor, *J. Phys. Chem. Lett.*, 2019, **10**, 6389–6398.

27 Z. Lebens-Higgins, D. O. Scanlon, H. Paik, S. Sallis, Y. Nie, M. Uchida, N. F. Quackenbush, M. J. Wahila, G. E. Sterbinsky, D. A. Arena, J. C. Woicik, D. G. Schlom and L. F. J. Piper, *Phys. Rev. Lett.*, 2016, **116**, 27602–27606.

28 Y. Park, S. W. Han, C. C. S. Chan, B. P. L. Reid, R. A. Taylor, N. Kim, Y. Jo, H. Im and K. S. Kim, *Nanoscale*, 2017, **9**, 10647–10652.

29 E. Lafalce, E. Amerling, Z.-G. Yu, P. C. Sercel, L. Whittaker-Brooks and Z. V. Vardeny, *Nat. Commun.*, 2022, **13**, 483.

30 A. Filippetti, P. Wadhwa, C. Caddeo and A. Mattoni, *Appl. Phys. Lett.*, 2022, **121**, 200501.

31 D. Niesner, M. Wilhelm, I. Levchuk, A. Osvet, S. Shrestha, M. Batentschuk, C. Brabec and T. Fauster, *Phys. Rev. Lett.*, 2016, **117**, 126401.

32 Z. Huang, S. R. Vardeny, T. Wang, Z. Ahmad, A. Chanana, E. Vetter, S. Yang, X. Liu, G. Galli, A. Amassian, Z. V. Vardeny and D. Sun, *Appl. Phys. Rev.*, 2021, **8**, 031408.

33 B. Wu, H. Yuan, Q. Xu, J. A. Steele, D. Giovanni, P. Puech, J. Fu, Y. F. Ng, N. F. Jamaludin, A. Solanki, S. Mhaisalkar, N. Mathews, M. B. J. Roeffaers, M. Gratzel, J. Hofkens and T. C. Sum, *Nat. Commun.*, 2019, **10**, 484.

34 Y.-K. Jung, M. Abdulla, R. H. Friend, S. D. Stranks and A. Walsh, *J. Mater. Chem. C*, 2022, **10**, 12560–12568.

35 G. Weng, J. Xue, J. Tian, X. Hu, X. Bao, H. Lin, S. Chen, Z. Zhu and J. Chu, *ACS Photonics*, 2018, **5**, 2951–2959.

36 T. Shen, J. Qin, Y. Bai, J. Zhang, L. Shi, X. Hou, J. Zi and B. Hu, *Opto-Electron. Adv.*, 2022, **5**, 200051.

37 Y. Bai, J. Qin, L. Shi, J. Zhang, M. Wang, Y. Zhan, H. Zou, S. Haacke, X. Hou, J. Zi and B. Hu, *Adv. Opt. Mater.*, 2019, **7**, 1900345–1900351.